AGU PUBLICATIONS

Geophysical Research Letters

RESEARCH LETTER
10.1002/2016GL068771

Key Points:
- The present-day (twentieth) MJO is stronger than the past (nineteenth) MJO by 33%
- Greenhouse gas forcing accounts for about 75% of the total changes in MJO strength
- SST warming over the equatorial Pacific and inverted Walker circulation induce the strength change

Correspondence to:
K.-H. Seo,
khseo@pusan.ac.kr

Citation:
Song, E.-J., and K.-H. Seo (2016), Past- and present-day Madden-Julian Oscillation in CNRM-CM5, *Geophys. Res. Lett.*, *43*, 4042–4048, doi:10.1002/2016GL068771.

Received 21 MAR 2016
Accepted 28 MAR 2016
Accepted article online 31 MAR 2016
Published online 30 APR 2016

Past- and present-day Madden-Julian Oscillation in CNRM-CM5

Eun-Ji Song[1] and Kyong-Hwan Seo[1]

[1]Department of Atmospheric Sciences, Division of Earth Environmental Systems, Pusan National University, Busan, South Korea

Abstract Madden-Julian Oscillation (MJO) in the past (nineteenth century) and present day (twentieth century) is examined using preindustrial and historical experiments of Centre National de Recherches Météorologiques-Coupled Models, version 5 (CNRM-CM5) in Coupled Model Intercomparison Project Phase 5 (CMIP5). The present-day MJO is stronger than the past MJO by 33% and it is ~10% more frequent. In particular, the MJO phases 4–7 signifying deep convection situated over the Maritime continent and western Pacific (WP) are considerably enhanced. These changes are due mainly to greenhouse gas forcing with little impact from nature forcing. Dynamical mechanisms for this change are investigated. A peculiar strengthening of MJO over WP comes from increased basic-state sea surface temperature (SST) over the Central Pacific (CP) and EP. The increase in precipitation over WP results from both the response to enhanced SST over CP and the inverted Walker circulation induced by the EP and CP SST increase. The latter causes a pair of anticyclonic Rossby waves straddling the equator, leading to moisture convergence over WP.

1. Introduction

Long-term changes or interdecadal variations of the Madden-Julian Oscillation (MJO) [*Madden and Julian*, 1994; *Zhang*, 2005], which is the most prominent physical mode in tropical intraseasonal variability, have been investigated by several studies. *Slingo et al*. [1999] and *Lee and Seo* [2011] showed that compared to the earlier period (before 1977), the recent period (after 1977) shows an increase in MJO amplitude by 17% to 20%. *Jones and Carvalho* [2006] demonstrated that MJO frequency increases from 3–4 to 4–5 events per year during 1948–2004.

In addition, climate simulations under future climate scenarios suggested the apparent increase in MJO activity during end of the 21st century [*Liu et al*., 2012; *Subramanian et al*., 2014; *Chang et al*., 2015]. These studies showed that MJO activity (in terms of wave power) increases by as much as 30–60% compared to end of the twentieth century. MJO frequency is estimated to rise to 5–6 events per year (about 25% increase) [*Jones and Carvalho*, 2011]. Due to the stronger activity in the future, MJO-induced teleconnection to higher latitudes is expected to strengthen [*Seo and Wang*, 2010; *Seo and Son*, 2012], implying the higher impacts on circulation, temperature, and precipitation anomalies in extratropical regions as well as tropics.

However, the MJO during the preindustrial period (the nineteenth century) has not been examined due to the scarcity of the observed or assimilated global data and difficulty in realistically simulating the MJO in climate models. Recent improvements in simulating the MJO, however, provide an opportunity to explore the characteristics of the MJO during this period. Using a superparameterized global climate model (CESM), *Arnold et al*. [2015] present a near double increase in intraseasonal outgoing longwave radiation variance between a preindustrial control run and a CO_2-quadrupling run. The Centre National de Recherches Météorologiques-Coupled Models, version 5 (CNRM-CM5) has been suggested as one of the best performing models among those participating in the phase 5 of the Coupled Model Intercomparison Project (CMIP5) [*Hung et al*., 2013] and the World Meteorological Organization's Working Group for Numerical Experimentation/Global Energy and Water Experiment Atmospheric System Study (WGNE and MJO–Task Force /GASS) global model comparison project [*Jiang et al*., 2015]. So the objective of this work is to estimate possible MJO changes during the past two centuries and to suggest dynamical mechanisms for these changes. In addition, a major contributor to the changes (and a resulting fraction explaining total variation) is presented by analyzing greenhouse forcing or natural forcing simulation output. Estimation of MJO activity for the past two centuries and warming future provides a whole picture of the changing MJO's strength and spatial properties.

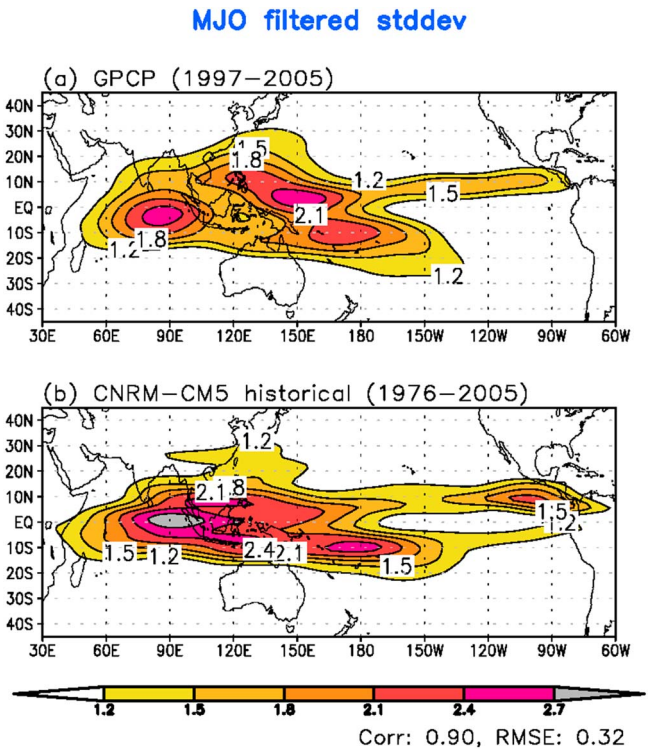

Figure 1. MJO-band filtered (wave numbers 1–5 and 30–90 days) variance in (a) GPCP (1997–2005) and (b) CNRM-CM5 historical precipitation (1976–2005). Contour intervals are 0.3 $mm^2\ day^{-2}$.

2. Model and Data

2.1. Model Description

This study uses the simulation output of CNRM-CM5, which includes ARPEGE-Climat (v5.2) as the atmosphere model, NEMO (v3.2) as the ocean model, Interaction Soil Biosphere Atmosphere as the land surface scheme, and GELATO (v5) as the sea ice model. OASIS (v3) system is employed as a coupler. Horizontal spectral resolution is T127 with 31 vertical levels following a progressive hybrid σ-pressure coordinate. The convective closure is based on the low-level moisture convergence scheme. More detailed information for CNRM-CM5 is found in *Voldoire et al.* [2013].

2.2. Simulation Output Types

Four simulation output are analyzed: (1) Pre-industrial control simulation (referred to as piControl) is integration with no changes in the external climate forcing set as year 1850 values. This simulation output corresponds to the past climate. (2) "Historical" is run with changes estimated by anthropogenic and natural forcing, and land use changes for the record period. This simulation is considered as the current climate, so it can be used to evaluate the model performance against observation. (3) "HistoricalNat" is a historical run imposed by only external natural forcing, which is solar and volcanic variability (SI and VI) forcing in CNRM-CM5. (4) "HistoricalGHG" is run forced with a time-evolving historic reconstruction of observed well-mixed greenhouse gases concentration. More experimental information is found in *Taylor et al.* [2009]. In this study, 30 years of data are analyzed for piControl during the period of 1870–1899 and for the other simulations during 1976–2005.

Except for historical run, all other simulations provide only seven variables in the current archive, which include precipitation, sea level pressure (SLP), surface temperature, surface specific humidity, maximum/minimum surface temperature, and maximum surface wind speed. Due to this limited availability in output variable, precipitation is used for MJO convective activity.

The difference between historical and piControl demonstrates changes due to the industrial effect, and that between historicalGHG (historicalNat) and piControl represents the effect of GHG (natural, respectively) forcing.

3. Results

3.1. Precipitation Simulated by CNRM-CM5

Again, in this study, only CNRM-CM5 is analyzed because it reproduces MJO characteristics (i.e., propagation and spectral peak) realistically [*Hung et al.*, 2013]. A prior examination of mean states shows that in general the mean states are properly represented in CNRM-CM5 historical runs (not shown). Figures 1a and 1b show the variance fields of the MJO-band precipitation in the Global Precipitation Climatology Project (GPCP) 1 daily (1DD) precipitation from 1997 to 2005 [*Huffman et al.*, 2001] and CNRM-CM5 historical run from 1976 to 2005. Using Lanczos filtering [*Duchon*, 1979], the MJO band signal is extracted for the wave with zonal wave numbers 1–5 and frequencies from 1/90 to 1/30 cpd in both symmetric and antisymmetric eastward propagating components as in *Wheeler and Kliadis* [1999]. CNRM-CM5 well simulates the strongest variance

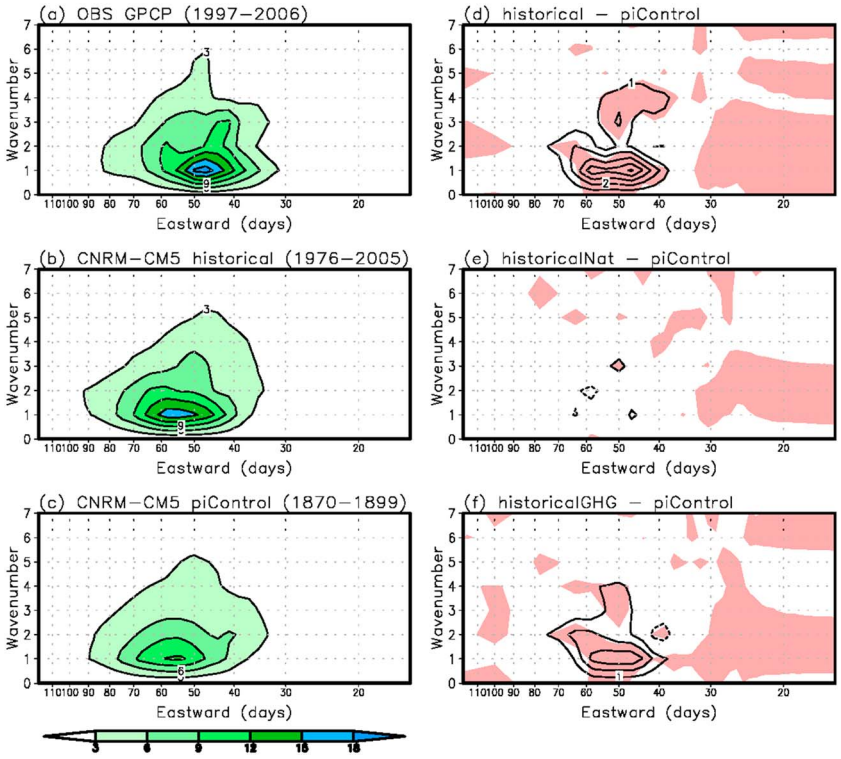

Figure 2. Wave number-frequency power spectra ($mm^2 day^{-2}$) for 30–90 day band-pass filtered precipitation averaged over 15°S–15°N from (a) GPCP (1997 to 2005), (b) historical (1976 to 2005), and (c) piControl (1870 to 1899). Differences in power between (d) historical and piControl, (e) historicalNat and piControl, and (f) historicalGHG and piControl. Figures 2a, 2b, and 2c have a unit of $mm^2 day^{-2}$. In Figures 2d, 2e, and 2f, contour interval is 1 $mm^2 day^{-2}$ and values above 90% confidence level based on two-tailed Student's *t* test are shaded.

in the warm pool and western Pacific similarly to the observation. The pattern correlation between the two fields is 0.90.

Figure 2 shows the space-time power spectra and differences. As shown in Figures 2a and 2b, CNRM-CM5 historical run simulates a peculiar, isolated MJO signal similar to the observation with a maximum power at zonal wave number 1. A slight underestimation is seen in power (from 18 to 15 $mm^2 day^{-2}$) and a major propagation speed is slowed by ~10 days (from 40–50 to 50–60 days). These findings suggest that CNRM-CM5 reproduces reasonably well the major features of the MJO (and the mean state).

3.2. The MJO in the Past and Present

Figure 2c shows that a domain of the strongest spectral peak in piControl is not different from historical (Figure 2c). They are located at periods of 50–60 days and zonal wave number 1. However, the peak amplitude of spectral power in piControl (12 $mm^2 day^{-2}$) weakens by ~33% compared to historical run (16 $mm^2 day^{-2}$). Such a substantial change is represented in Figure 2d, where a statistically significant difference in wave power is concentrated on the range of 40–70 days and wave numbers 1–2. Therefore, the MJO has been strengthened since the late-1800s due to the intensifying global warming.

To investigate a major cause of this increase in the present climate, difference in power spectra of historicalNat and historicalGHG with piControl is calculated (Figures 2e and 2f). It is evident that natural forcing has little influence on this change (Figure 2e), whereas the GHG forcing simulation has a remarkably similar pattern (Figure 2f) to that from all forcing (Figure 2d). This indicates that the MJO changes during the past century are mainly caused by the GHG forcing. The conclusion is also supported by another independent model in CMIP5 (e.g., IPSL-CM5A-LR, not shown). Calculation of changes in power due to GHG forcing and total forcing suggests that the GHG forcing-induced change explains as much as 75% of total spectral power variation. Natural forcing contributes to the change by only 6%.

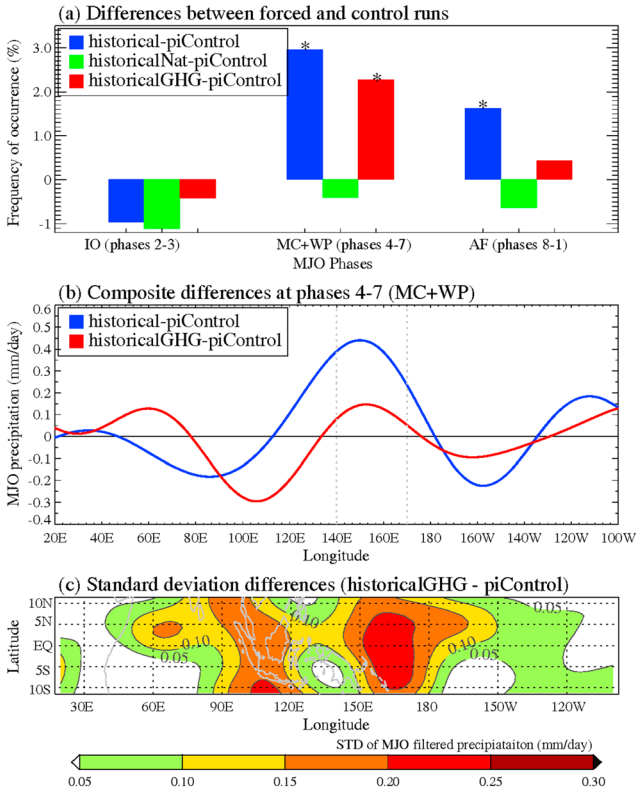

Figure 3. Differences in (a) frequency of occurrence of MJO events for different phases, (b) composite fields of the MJO-band-filtered (wave numbers 1–5 and 30–90 days) precipitation averaged over (10°S–10°N) at phases 4–7, and (c) standard deviation of the MJO-band-filtered precipitation between historicalGHG and piControl runs. Asterisks in Figure 3a denote significant changes at the 95% confidence level. Blue, green, and red bars represent changes of historical, historicalNat, and historicalGHG from piControl, respectively. Blue (red) line in Figure 3b indicates precipitation changes averaged over (10°S–10°N) at phases 4–7 in historical (historicalGHG) from piControl.

Changes in frequencies of MJO events between the two periods are calculated by selecting an MJO event using the following five conditions according to *Jones* [2009] and *Arnold et al.* [2015]: (1) an MJO amplitude is always larger than 0.35; (2) it propagates to the east so the daily longitudinal displacement is greater than 0° and less than 30°; (3) the entire duration of the event is greater than 30 days; (4) the average amplitude of the event is greater than 0.8; and (5) if moving distance of the event is greater than 360°, it is counted as a multiple MJO event. The numbers of MJO events for piControl, historical, historicalNat, and historicalGHG are 107, 117, 102, and 123. The present-day MJO is about 10% more frequent compared to the past.

To examine a more detailed property of changes in MJO activity, differences in the frequency of occurrence between each of individual forced runs and piControl for different MJO phases are plotted in Figure 3a. The frequency of occurrence is defined as a ratio of MJO active days to the total days, where the active day has an MJO amplitude larger than 1.0. For the consistent analysis across all simulation outputs, MJO amplitude indices are reconstructed by time series of coefficients produced by projecting the anomaly fields onto the empirical orthogonal function pattern for GPCP data averaged over 30°S–30°N. A notable increase in active day frequency in the historical and historicalGHG runs (blue and red bars in Figure 3a) is seen for phases 4–7 (referred as the Maritime continent (MC) + western Pacific (WP) phase), which exceeds the 95% confidence level estimated by a Monte Carlo test based on 1000 random samplings. Even for phases 8 and 1 the historical run shows a significant increase. On the contrary, a slight or moderate decrease appears for phases 2–3, which is statistically insignificant. Phases 4–7 represent the enhanced precipitation located over the Maritime continent and the western Pacific.

The spatial distribution in changes of precipitation on the intraseasonal band for phases 4–7 (blue line in Figure 3b) suggests the significant increase in this quantity over the Maritime continent and the western Pacific (100°–180°E) and decrease over the central IO. A similar increase of the MJO precipitation in the historical run is seen in the composite field of precipitation for phases 8–1 over the equatorial African region (not shown). In particular, it is evident that for this MC + WP phase, the increased frequency in active day is mainly due to the GHG forcing (see red bar in Figure 3a). The natural forcing affects little (green bar in Figure 3a). Similar to the total (historical) forcing (blue line in Figure 3b), the GHG forcing-induced increase in precipitation appears over the WP region (red line in Figure 3b). The significant increase in precipitation frequency (Figure 3a) and strength (Figure 3b) in the current climate for phases 4–7 is confirmed by the difference in variance of intraseasonal precipitation (which represents changes in both strength and frequency) between historicalGHG and piControl as shown in Figure 3c, which demonstrates that the peak increase of intraseasonal precipitation variability occurs over (140°–170°E), as similarly as in the red line of Figure 3b. All these indicate that GHG forcing leads to an enhanced MJO convection over the WP region.

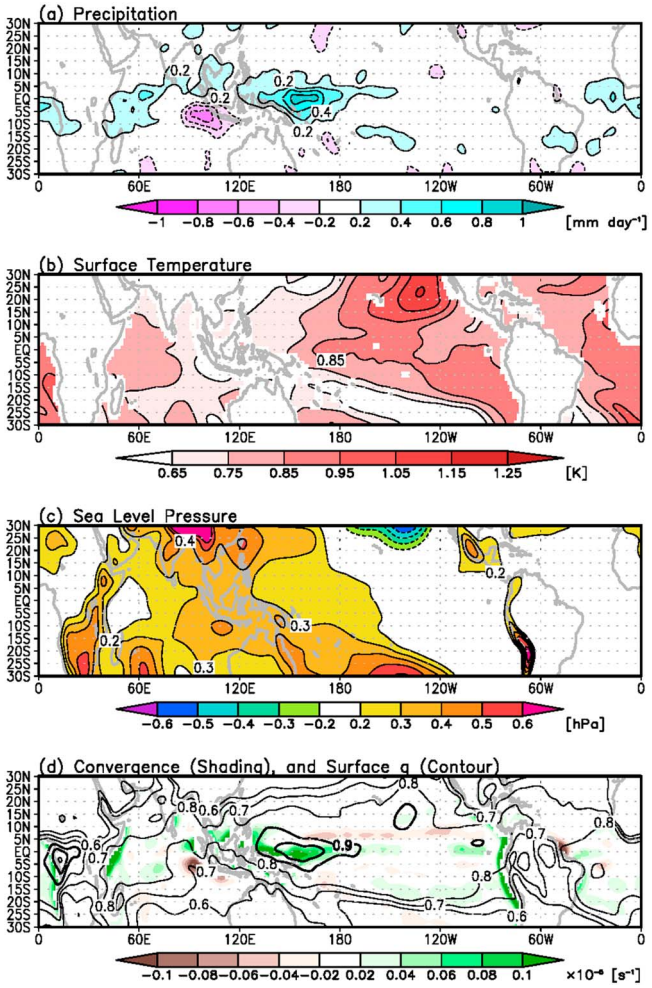

Figure 4. Differences between historicalGHG and piControl of the annual mean (a) precipitation, (b) surface temperature, (c) SLP, and (d) surface specific humidity (contour) and SLP-driven convergence (shading).

3.3. Dynamical Mechanisms for MJO Changes Due to GHG Forcing

Then, a question arises as to how this increase in MJO convection appears over the WP region. For this, differences in basic states between historicalGHG and piControl are presented in Figure 4, where the increase of the precipitation is seen over the WP (Figure 4a). This area is exactly the same area where variance of the MJO-band-filtered precipitation is maximized. As in *Maloney and Xie* [2013], processes resulting in changes of the mean precipitation are likely to work for inducing changes in intraseasonal precipitation variability.

Sea surface temperature (SST) changes by GHG forcing also appears as the El Niño-like warming structure (Figure 4 b). A signal representing the enhancement of Central Pacific (CP)-type El Niño is prominent with a widespread positive SST difference field over the EP. This pattern is in agreement with the observed SST difference measured with Extended Reconstructed SST (ERSST v3). Also, in some sense, this SST pattern has some similarity with changes in the 21st century due to the global warming in CMIP future simulation data [e.g., *Yeh et al.*, 2012]. This CP SST induces the positive precipitation over the WP shown in Figure 4a. However, beside of this direct SST forcing from the CP SST area, there seems an indirect contribution to this precipitation increase in the WP. That is, due to the SST increase in the CP and EP, the Walker circulation weakens, leading to downward motion over the MC and Eastern IO so that an increase in SLP develops over those regions as shown in Figure 4c. The suppressed convection region induces the anticyclonic off-equatorial Rossby waves, which act to generate moisture convergence over the WP (Figure 4d). The wind convergence estimated from the SLP field [*Stevens et al.*, 2002; *Back and Bretherton*, 2009; *Maloney and Xie*, 2013] shows the clear collocation of the convergence area with that of increase in the precipitation over this WP (Figure 4a). The surface moisture also increases in this area (Figure 4d). It is of interest to notice a significant reduction in the precipitation over the southeastern tropical IO; this is attributed by the sinking motion of the reversed Walker circulation forced by the Pacific SST increase.

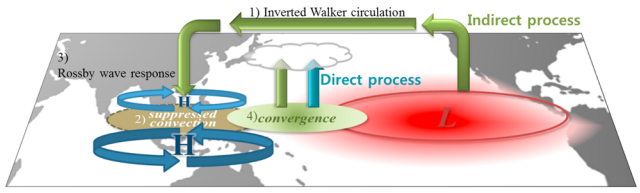

Figure 5. Schematic diagrams illustrating the dynamical mechanisms for the increase of precipitation over the WP due to GHG forcing.

The processes involved in this increase in the precipitation over the WP are presented in Figure 5. To sum, the GHG forcing results in the increases in convective activity of both the MJO and mean state over the WP. These increases come from the enhanced CP SST forcing and inverted Walker circulation with the latter producing Rossby wave response in both sides of the

subtropics and ensuing moisture convergence over the WP. However, the question of which mechanism prevails is not addressed in this study.

4. Summary and Discussion

In this study, the past- (nineteenth century) and present-day (twentieth century) MJO is compared. The current MJO is stronger than the past MJO by as much as 33% and it is about 10% more frequent. In particular, the MJO phases 4–7 signifying deep convection located over the Maritime continent and western Pacific are considerably enhanced. These changes are mainly due to GHG forcing (explaining 75% of changes from total forcing) with the nature forcing producing little impact. A different model in CMIP5 also shows the similar results. Note that if considering that a wave power increases by ~50% between the ends of the 20th and 21st centuries, strength of the MJO in the future climate will be nearly doubled compared to the end of the nineteenth century.

Dynamical mechanisms for an increase in MJO variance over the WP is explained by differences in mean states between the past- and present-day climates. This increase arises from the increased SST over the CP and EP regions during the current period compared to the past. In response to the enhanced SST over the CP, precipitation over the WP increases. Meanwhile, the inverted Walker circulation induced by the EP and CP SST increase in the present-day climate generates suppressed convection over the MC and southwestern IO, leading to a pair of anticyclonic Rossby waves straddling the equator and the low-level moisture convergence over the WP.

This result is of great implication in interpreting the recent studies on the present-day and future MJO and its impact. For example, *Yoo et al*. [2011] reported more enhanced MJO activity for the phases 4–6 during 1994–2008 compared to 1979–1993, which through the increased poleward Rossby wave propagation, contributes to amplification of the Arctic warming in recent years. Likewise, *Subramanian et al*. [2014] showed in the CMIP5 warmest global warming projection that future MJO is expected to have a much stronger convection anomaly over the WP for phases 4–6. Hence, as in the present study, these share the same feature: enhancement in convective activity over the WP as time progresses. Impacts of the warming SST over the equatorial Pacific and Indian Ocean on the MJO or feedback between atmosphere-ocean should be elucidated more in detail in the future.

Acknowledgments

This work was funded by the Korea Meteorological Administration Research and Development Program under grant KMIPA 2015-2113 and National Research Foundation of Korea (NRF) grant by the Korea government (MSIP) (NRF-2015R1A2A2A01006663). The authors would like to acknowledge the support from the Korea Institute of Science and Technology Information (KISTI). We acknowledge the World Climate Research Programme's Working Group on Coupled Modeling, which is responsible for CMIP, and we thank the climate modeling groups including CNRM-CERFACS and IPSL. For CMIP the U.S. Department of Energy's Program for Climate Model Diagnosis and Intercomparison provides coordinating support and led development of software infrastructure in partnership with the Global Organization for Earth System Science Portals. We thank the two reviewers for their helpful comments and suggestions, which improved manuscript.

References

Arnold, N. P., M. Branson, Z. Kuang, D. A. Randall, and E. Tziperman (2015), MJO intensification with warming in the superparameterized CESM, *J. Clim.*, *28*, 2706–2724.

Back, L. E., and C. S. Bretherton (2009), On the relationship between SST gradients, boundary layer winds, and convergence over the tropical oceans, *J. Clim.*, *22*, 4182–4196.

Chang, C.-W. J., W.-L. Tseng, H.-H. Hsu, N. Keenlyside, and B.-J. Tsuang (2015), The Madden-Julian Oscillation in a Warming World, *Geophys. Res. Lett.*, *42*, 6034–6042, doi:10.1002/2015GL065095.

Duchon, C. E. (1979), Lanczos filtering in one and two dimensions, *J. Appl. Meteorol.*, *18*, 1016–1022.

Huffman, G. J., R. F. Adler, M. M. Morrssey, S. Curtis, R. Joyce, B. McGavock, and J. Susskind (2001), Global precipitation at one-degree daily resolution from multisatellite observations, *J. Hydrometeorol.*, *2*, 36–50.

Hung, M.-P., J.-L. Lin, W. Wang, D.-H. Kim, T. Shinoda, and S. J. Weaver (2013), MJO and convectively coupled equatorial waves simulated by CMIP5 climate models, *J. Clim.*, *26*, 6185–6214.

Jiang, X., et al. (2015), Vertical structure and physical processes of the Madden-Julian oscillation: Exploring key model physics in climate simulations, *J. Geophys. Res. Atmos.*, *120*, 4718–4748, doi:10.1002/2014JD022375.

Jones, C. (2009), A homogeneous stochastic model of the Madden-Julian Oscillation, *J. Clim.*, *22*, 3270–3288.

Jones, C., and L. Carvalho (2006), Changes in the activity of the Madden-Julian oscillation during 1958–2004, *J. Clim.*, *19*, 6353–6370.

Jones, C., and L. Carvalho (2011), Will global warming modify the activity of the Madden-Julian oscillation?, *Q. J. R. Meteorol. Soc.*, *137*, 544–552.

Lee, S.-H., and K.-H. Seo (2011), A multi-scale analysis of the interdecadal change in the Madden–Julian Oscillation, *Atmos. Korean Meteorol.*, *21*(2), 143–149.

Liu, P., T. Li, B. Wang, M. Zhang, J.-J. Luo, Y. Masumoto, X. Wang, and E. Roeckner (2012), MJO change with A1B global warming estimated by the 40-km ECHAM5, *Clim. Dyn.*, doi:10.1007/s00382-012-1532-8.

Madden, R. A., and P. Julian (1994), Observations of the 40–50-day tropical oscillation—A review, *Mon. Weather Rev.*, *122*, 814–837.

Maloney, E. D., and S.-P. Xie (2013), Sensitivity of tropical intraseasonal variability to the pattern of climate warming, *J. Adv. Model. Earth Syst.*, *5*, 32–47, doi:10.1029/2012MS000171.

Seo, K.-H., and S.-W. Son (2012), The global atmospheric circulation response to tropical diabatic heating associated with the Madden-Julian oscillation during northern winter, *J. Atmos. Sci.*, *69*, 79–96.

Seo, K.-H., and W. Wang (2010), The Madden-Julian Oscillation simulated in the NCEP climate forecast system model: The importance of stratiform heating, *J. Clim.*, *23*, 4770–4793.

Slingo, J. M., D. P. Rowell, K. R. Sperber, and F. Nortley (1999), On the predictability of the interannual behaviour of the Madden-Julian oscillation and its relationship with El Niño, *Q. J. R. Meteorol. Soc.*, *125*, 583–609.

Stevens, B., J. J. Duan, J. C. McWilliams, M. Münnich, and J. D. Neelin (2002), Entrainment, Rayleigh friction, and boundary layer winds over the tropical Pacific, *J. Clim.*, *15*, 30–44.

Subramanian, A., M. Jochum, A. J. Miller, R. Neale, H. Seo, D. Waliser, and R. Murtugudde (2014), The MJO and global warming: A study in CCSM4, *Clim. Dyn.*, *42*, 2019–2031.

Taylor, K. E., R. J. Stouffer, and G. A. Meehl (2009), A summary of the CMIP5 experiment design, PCDMIRep. [Available online at http://cmip-pcmdi.llnl.gov/cmip5/docs/Taylor_CMIP5_design.pdf.]

Voldoire, A., et al. (2013), The CNRM-CM5.1 Global climate model: Description and basic evaluation, *Clim. Dyn.*, *40*, 2091–2121.

Wheeler, M., and G. N. Kliadis (1999), Convectively coupled equatorial waves: Analysis of clouds and temperature in the wavenumber-frequency domain, *J. Atmos. Sci.*, *56*, 374–399.

Yeh, S.-Y., Y.-G. Ham, and J.-Y. Lee (2012), Changes in the tropical Pacific SST trend from CMIP3 to CMIP5 and its implication of ENSO, *J. Clim.*, *25*, 7764–7771.

Yoo, C., S. Feldstein, and S. Lee (2011), The impact of the Madden-Julian Oscillation trend on the Arctic amplification of surface air temperature during the 1979–2008 boreal winter, *Geophys. Res. Lett.*, *38*, L24804, doi:10.1029/2011GL049881.

Zhang, C. (2005), Madden-Julian oscillation, *Rev. Geophys.*, *43*, RG2003, doi:10.1190/1.1988182.